Dalton Transactions

PAPER

View Article Online
View Journal | View Issue

Cite this: *Dalton Trans.*, 2019, **48**, 6421

Phosphonate-assisted tetranuclear lanthanide assemblies: observation of the toroidic ground state in the Tb^{III} analogue†

Sourav Biswas,‡[a] Pawan Kumar,‡[b] Abinash Swain,[c] Tulika Gupta,[c] Pankaj Kalita,[d] Subrata Kundu,[b] Gopalan Rajaraman *[c] and Vadapalli Chandrasekhar *[b,e]

The reaction of $LnCl_3{\cdot}6H_2O$ with a multidentate flexible Schiff base ligand (LH_4), $H_2O_3P^tBu$ and trifluoroacetic acid (tfaH) afforded a series of homometallic tetranuclear complexes, $[Ln_4(LH_2)_2(O_3P^tBu)_2(\mu_2\text{-}\eta^1\eta^1tfa)_2][2Cl]$ (Ln = Dy^{III} (**1**), Tb^{III} (**2**) and Gd^{III} (**3**)). The tetranuclear lanthanide core contains two structurally different lanthanide centres, one being in a distorted trigonal dodecahedron geometry and the other in a distorted trigonal prism. Complexes **1–3** were investigated *via* direct and alternating current (DC and AC) magnetic susceptibility measurements. Only **1** revealed a weak single-molecule magnet (SMM) behaviour. Alternating current (ac) magnetic susceptibility measurements on **1** reveal a frequency-dependent out-of-phase signal. However, the absence of distinct maxima in the χ'' peak (within the temperature/frequency range of our experiments) prevented deduction of the experimental energy barrier for magnetization reversal (U_{eff}) and the relaxation time. We have carried out extensive *ab initio* (CASSCF + RASSI-SO + SINGLE_ANISO + POLY_ANISO) calculations on complexes **1–2** to gain deeper insights into the nature of magnetic anisotropy. Our calculations yielded only one exchange coupling parameter between the two Ln^{III} centres bridged by the ligand (neglecting the exchange between the Ln^{III} centres that are not proximal wrt each other). All the extracted J values indicate a weakly antiferromagnetic coupling between the metal centres (J = −0.025 cm^{-1} for **1** and J = −0.015 cm^{-1} for **2**). Calculated exchange coupled U_{cal} values of ~5 and ~1 cm^{-1} in **1** and **2** respectively nicely corroborated the experimental observations regarding weak and no SMM characteristics. Our calculations indicated the presence of a net single-molecule toroidal (SMT) behaviour in complex **2**. On the other hand, fitting the magnetic data (susceptibility and magnetization) in the isotropic cluster **3** revealed weak AFM exchange couplings of J_1 = 0.025 cm^{-1} and J_2 = −0.020 cm^{-1} which are consistent with those for Gd^{III} ions.

Received 8th February 2019,
Accepted 2nd April 2019

DOI: 10.1039/c9dt00592g

rsc.li/dalton

Introduction

Research on lanthanide complexes is experiencing an unprecedented renaissance in view of the potential applications of many of these compounds in molecular materials in general and molecular magnets in particular.[1] Owing to the fact that a number of lanthanide ions have a large spin–orbit coupling and a reasonably large ground-state spin, two factors that are deemed important in the design of single-molecule magnets, lanthanide complexes are being increasingly investigated for their single-molecule magnet (SMM) behaviour.[2] The latter is characterized by the blocking of magnetization below a certain blocking temperature (T_B).[3] Furthermore, SMMs are characterized by a double-well energy potential with an effective energy barrier (U_{eff}).[3] Multiple mechanisms of relaxation of magnetization are known which include Orbach, Raman and quantum tunnelling processes.[4] In addition to SMMs, in recent years, there has also been attention on single molecule toroics

[a]*Department of Geo-Chemistry, Keshav Deva Malaviya Institute of Petroleum Exploration, Dehradun-248915, India*
[b]*Department of Chemistry, Indian Institute of Technology Kanpur, Kanpur-208016, India. E-mail: vc@iitk.ac.in*
[c]*Department of Chemistry, Indian Institute of Technology Bombay, Powai, Mumbai 400076, India. E-mail: rajaraman@chem.iitb.ac.in*
[d]*School of Chemical Sciences, National Institute of Science Education and Research Bhubaneswar, HBNI, Jatni, Khurda – 752050, India*
[e]*Tata Institute of Fundamental Research, Gopanpally, Hyderabad 500 107, India. E-mail: vc@tifrh.res.in*

†Electronic supplementary information (ESI) available: Molecular structure, bond lengths and bond angles of **2** and **3**. Supramolecular interactions, crystal packing of **1** in the *X*, *Y*, and *Z* direction, CASSCF + RASSI-SO + SINGLE_ANISO computed energies of the eight low-lying KDs and SINGLE_ANISO computed crystal field parameters **1** and **2**. The *ab initio* calculated magnetization relaxation mechanism for (a) Dy1/Dy3 and (b) Dy2/Dy4 centres respectively in **1**. Field dependence of the molar magnetization plot at 2 K and field dependence of the molar magnetization plot in complexes. Temperature dependence of the (a) in-phase and (b) out-of-phase ac susceptibility of **1** and **2** in the presence of zero and biased field. CCDC 1556047–1556049. For ESI and crystallographic data in CIF or other electronic format see DOI: 10.1039/c9dt00592g

‡These authors contributed equally to this work.

where the arrangement of the individual moments around the metal ions leads to an overall toroidal moment because of a wheel-like topology.[5a–d] Since the toroidal nature can be manipulated by means of an electric field, such compounds have the potential to be used as multiferroic materials.[5e]

Among the various types of homometallic lanthanide complexes studied thus far the structural range has been quite impressive.[2,6] The nuclearity has also varied from 1 to 60.[6] Among such complexes, we have been focusing on tetranuclear complexes and have found that depending on the type of structure the details of the SMM behaviour vary considerably.[7] Several types of molecular topologies are now known among the tetranuclear complexes: square-grid,[8a–c] cubane,[8d] tetragonal planar,[8e] Y-shaped,[8f] rhombus,[8g] see-saw,[8h] linear,[8i,j] *etc*. In addition to very interesting structural features, such complexes also reveal fascinating magnetic properties such as multi-step relaxation of magnetization.[8g,9] Thus, in a rhombus-shaped complex two different U_{eff} values were extracted and were correlated with distinct coordination environments and coordination geometries around the lanthanide ions.[8g] More recently we have observed an interesting toroidal magnetic moment in $[Dy_4(LH)_2(\mu_2\text{-}\eta^1\eta^1\text{Piv})(\eta^2\text{-Piv})(\mu_3\text{-OH})_2]$ [LH_4 = 6-((bis(2-hydroxyethyl)amino)methyl)-*N*′-(2-hydroxy-3-methoxybenzylidene)picolino-hydrazide].[2g] Examples from the literature reveal that $[Dy_4(\mu_3\text{-OH})_2(bmh)_2(msh)_4Cl_2]$[10] (bmh = 1,2-bis(2-hydroxy-3-methoxybenzylidene)hydrazone; msh = methoxysalicylaldehyde hydrazone) and $[Dy_4K_2O(O^tBu)_{12}]$[4b] possess exceptionally high energy barriers for magnetization reversal.

One of the challenges in the preparation of multi-nuclear complexes with distinct structures and nuclearity is the lack of reliable synthetic methods. Moreover, SMT demands to have an arrangement where all the spin centres reside in a plane with a closed loop structure. From a synthesis point of view, aroyl hydrazine based ligands are very promising in view of their capability of directing all the lanthanide centres in a planar arrangement with assistance from enolisable oxygen.[5a–d] We have pioneered the use of phosphonate ligands for the preparation of lipophilic transition metal ensembles.[11a] The versatile coordination modes and strong binding capabilities of the phosphonate and organophosphate family of ligands result in a variety of 3d,[11b] 3d–4f[11a] and 4f[11a] assemblies with interesting properties such as proton conduction,[11c,d] magnetic refrigerants,[11e–i] *etc*. It was of interest to us to examine if suitable phosphonate ligands can be deployed as co-ligands in assembling polynuclear lanthanide complexes. A perusal of the literature revealed that the use of phosphonate ligands in lanthanide chemistry has been sparse. However, the available examples, Ln_4P_4,[12a] Ln_4P_2,[12b] Ln_8P_6 [12c] and $Ln_{10}P_6$,[12d] already point to the interesting synthetic possibilities that exist for using the phosphonate ligands.

Accordingly, in the following, we report our findings on the use of a multi-component synthetic strategy involving a lanthanide salt, a phosphonate ligand, a trifluoroacetate (tfa) ligand and a multi-site-coordination ligand, LH_4. Thus, the reaction of LH_4, (LH_4 = 6-((bis(2-hydroxyethyl)amino)methyl)-*N*′-((8-hydroxyquinolin-2-yl)methylene)picolinohydrazide), $LnCl_3{\cdot}6H_2O$, $H_2O_3P^tBu$ and tfaH in the presence of triethylamine in the stoichiometric ratio 1 : 2 : 1 : 1 : 4 afforded homometallic tetranuclear complexes, $[Ln_4(LH_2)_2(O_3P^tBu)_2(\mu_2\text{-}\eta^1\eta^1tfa)_2]{\cdot}2Cl{\cdot}x\text{MeOH}{\cdot}y\text{H}_2\text{O}$ [**1**, Ln = Dy^{III}, x = 2, y = 2; **2**, Ln = Tb^{III}, x = 2, y = 2; **3**, Ln = Gd^{III}, x = 2, y = 2] (Scheme 1). The synthesis, molecular structure and magnetic properties of **1–3** and *ab initio* studies of **1–2** are described herein.

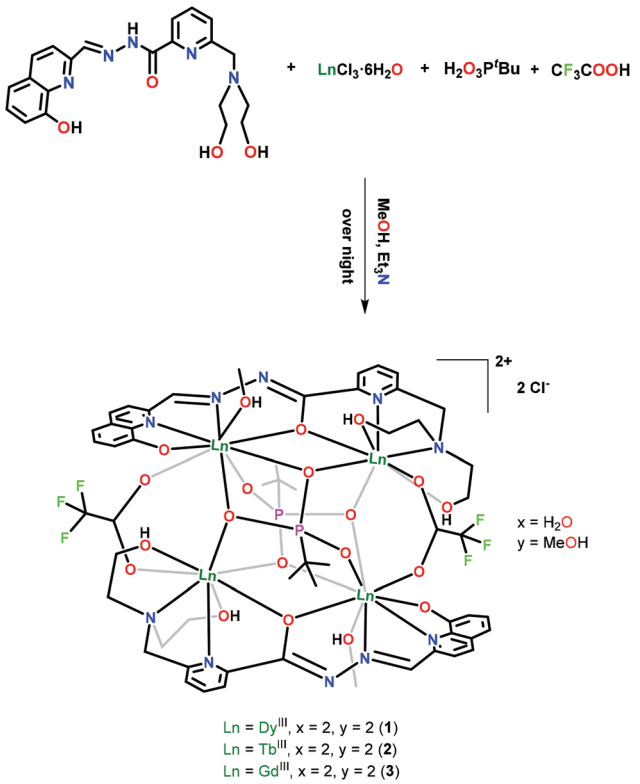

Scheme 1 Synthesis of Ln_4 complexes **1–3**.

Results and discussion

Synthetic aspects

Aroyl hydrazine-based multidentate Schiff base ligands have been shown to be quite effective in assembling homometallic lanthanide complexes.[7–9] Utilizing flexible features such as keto–enol tautomerism[13] in ligands such as (6-hydroxymethyl)-*N*′-((8-hydroxyquinolin-2-yl)methylene)picolinohydrazide, we have previously assembled a series of rhombus-shaped Ln_4 complexes, $[(LH)_2Ln_4(\mu_2\text{-O})_4(H_2O)_8]$ (Ln = Dy^{III} and Ho^{III}) (Scheme 2) whose Dy^{III} analogue exhibited SMM behaviour with a two-step relaxation of magnetisation.[8g]

Motivated by the above result, we have customized the above ligand further with the replacement of the pendant –CH_2OH group by a diethanolamine arm while keeping the rest of the skeleton intact. Complexes thus formed from this ligand will be devoid of the exogenous O^{2-} group. The choice of the diethanolamine group is based on literature precedence,[2g,h] which reveals that in its protonated form, this

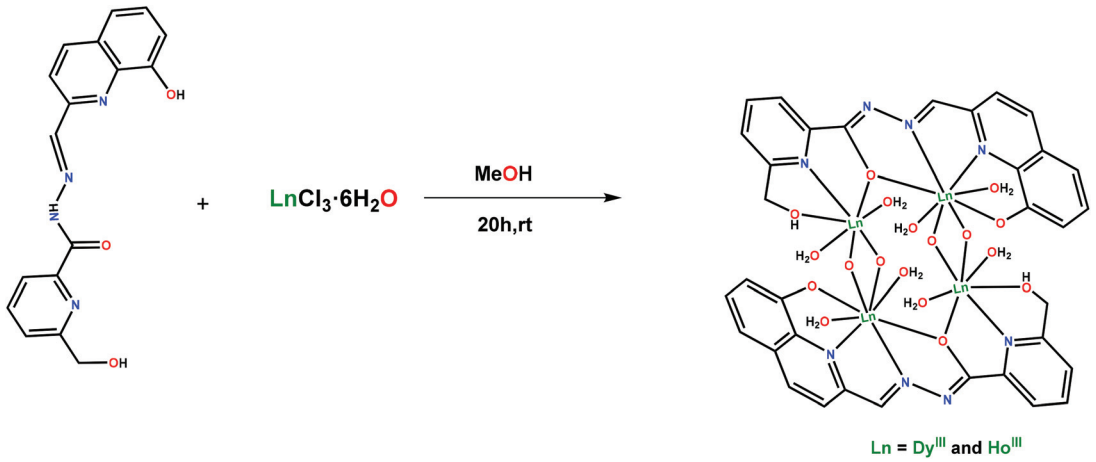

Scheme 2 Synthesis of rhombus-shaped $[(LH)_2Ln_4(\mu_2\text{-}O)_4(H_2O)_8]$.[8g]

arm can serve as a chelating ligand, while in its deprotonated form it can function as a potential bridging ligand among the metal centres. The ligand LH_4 was prepared by following a two-step synthetic protocol which involves the synthesis of G5 and subsequent reaction with 8-hydroxyquinoline-2-carbaldehyde to afford the final ligand, LH_4 (Scheme 3).

The multidentate flexible ligand LH_4 contains divergent coordination sites: in its doubly deprotonated form two unsymmetrical coordination pockets can be discerned, one of these is tetradentate and comprises a hydroxy, a 8-hydroxyquinoline pyridine, an imine N, and hydrazine O while the other is pentadentate, consisting of a common hydrazone oxygen, a diethanolamine and a pyridine N (Fig. 1). We anticipated that $[LH_2]^{2-}$ would be able to encapsulate two lanthanide ions affording a dinuclear motif which can be bridged by two phosphonate ligands to afford a tetranuclear compound. The use of phosphonate ligands in bridging dimeric motifs and affording

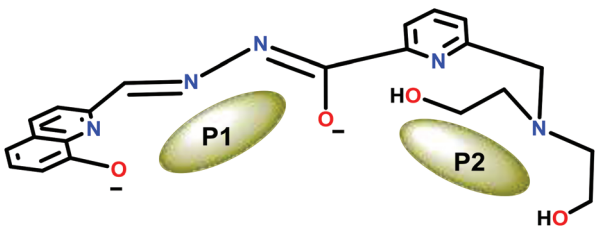

Fig. 1 The two potential coordination pockets of $[LH_2]^{2-}$.

tetranuclear complexes has been shown by us in several instances involving transition metal chemistry.[11a] We also used trifluoroacetic acid (tfaH) with the intention of utilizing the bridging coordination capability of tfa. Accordingly, the reaction of LH_4, $LnCl_3{\cdot}6H_2O$, $H_2O_3P^tBu$ and tfaH in the presence of triethylamine with the stoichiometric ratio of

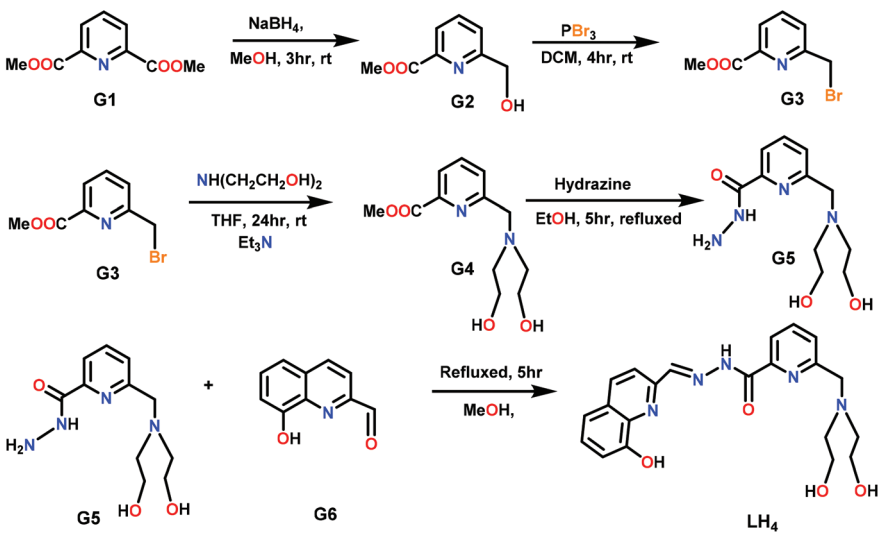

Scheme 3 Synthesis of LH_4.

1 : 2 : 1 : 1 : 4 fostered the formation of homometallic tetranuclear complexes, $[Ln_4(LH_2)_2(O_3P^tBu)_2(\mu_2\text{-}\eta^1\eta^1tfa)_2]\cdot 2Cl\cdot x MeOH\cdot yH_2O$ [**1**, Ln = Dy^{III}, x = 2, y = 2; **2**, Ln = Tb^{III}, x = 2, y = 2; **3**, Ln = Gd^{III}, x = 2, y = 2].

X-ray crystallography

X-ray diffraction study reveals that complexes **1–3** are isostructural and dicationic and crystallize in a triclinic system in the space group $P\bar{1}$ with Z = 1. Each of the three complexes contains two chloride counter anions to compensate for the overall charge. The asymmetric unit of these complexes comprises one-half of the total molecule *viz*. $[Dy_2(LH_2)(t\text{-}BuPO_3)(tfa)][Cl]$

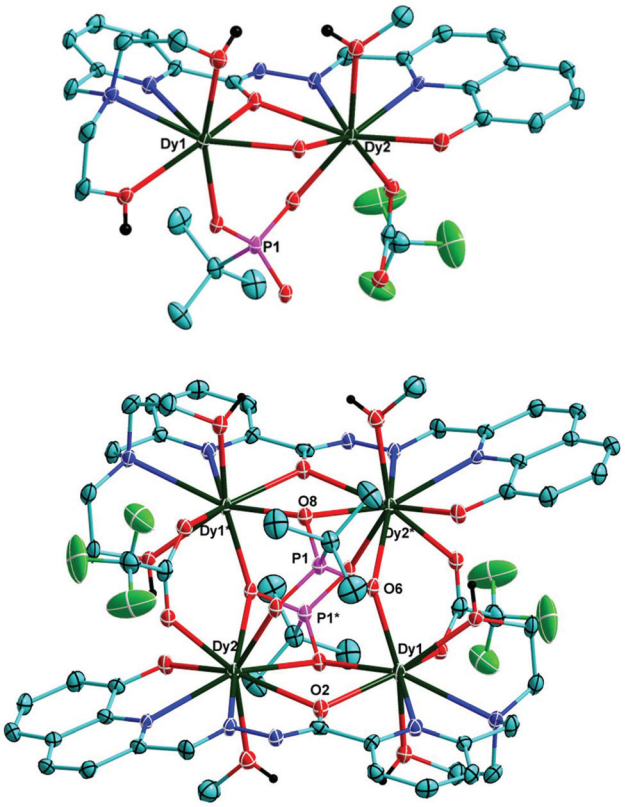

Fig. 2 Asymmetric unit (top) and molecular structure (bottom) of **1** as thermal ellipsoids at 50% probability level (selected hydrogen atoms, chlorides and the solvent molecules have been omitted for clarity). Colour codes: N = blue; O = red; C = aqua; Dy = dark green; P = pink; F = bright green and H = black.

and the full molecule is generated as a result of an inversion centre inside the molecule (Fig. 2(top)). In view of their similarity, we describe the molecular structure of **1** as a representative example. A perspective view of **1** is given in Fig. 2(bottom) and those of **2** and **3** are given in the ESI (Fig. S1 and S2†). Selected bond lengths and bond angles of **1** are given in Table 1 while those of **2** and **3** are given in Tables S1 and S2.†

The homometallic tetranuclear ensemble in **1** is assembled in the following manner. First, the enol form of $[LH_2]^{2-}$ encapsulates two lanthanide ions in its two coordination pockets, P1 (2O, 2N) and P2 (3O, 2N) (Fig. 1). The enolate oxygen of the ligand forms a bridge between the two lanthanide centres to generate the dimeric subunit $[Dy_2(LH_2)]^{4+}$. Two such dimeric subunits are stitched together by two doubly deprotonated $t\text{-}BuPO_3^{2-}$ and two tfa ligands to afford the homometallic tetranuclear complex **1** (Fig. 2). While each of the phosphonate ligands binds to all four lanthanide centres in a μ_4 binding mode the two tfa ligands are involved in bridging a pair of lanthanide ions belonging to the two sub-units. The coordination mode of the phosphonate ligand is reminiscent of its behaviour in transition metal complexes as exemplified in Fig. 3. Thus, the cumulative and varied binding modes of $[LH_2]^{2-}$, $[t\text{-}BuPO_3]^{2-}$ and tfa (Fig. 3) make the assembly of **1** possible.

The tetranuclear assembly can be envisioned as a tetragonally compressed octahedron whose basal plane (rectangle) is formed by the four coplanar Dy^{III} (Dy1, Dy1*, Dy2 and Dy2*) while the two axial vertices are constructed by the two P (P1 and P1*) of the two $t\text{-}BuPO_3^{2-}$ ligands which are displaced 1.98 Å on either side of the basal plane (Fig. 4a). Further analysis of the molecular structure of **1** reveals some interesting features. The basal plane can be categorized as a rectangle as deduced from the two equal bond distances, Dy1–Dy2 = 4.059 Å and Dy1–Dy2* = 4.232 Å. Interestingly, the inclusion of the enolate oxygen in the core renders it an approximately rugby-ball shaped topology (Fig. 4b).

1 contains two different types of Dy^{III} centres: Dy1 and Dy1* are eight-coordinated and are surrounded by a similar coordination environment (6O, 2N) and possess a distorted trigonal dodecahedron geometry whereas both Dy2 and Dy2* are nine-coordinated in a distorted tricapped trigonal prismatic geometry (7O, 2N) (Fig. 5).

The Dy–O bond lengths fall in a very narrow range, 2.346–2.392 Å. In contrast, $Dy\text{–}O_{phosphonate}$ bond lengths lie in

Table 1 Selected bond distances (Å) and bond angles (°) of **1**

Bond distances around Dy1		Bond distances around Dy2		Dy(2)–O(6)*	2.651(4)
Dy(1)–O(6)	2.285(4)	Dy(2)–O(7)	2.250(4)		
Dy(1)–O(4)	2.334(4)	Dy(2)–O(1)	2.347(4)	Bond angles around Dy	
Dy(1)–O(9)	2.343(4)	Dy(2)–O(3)	2.381(4)	Dy(1)–O(6)–Dy(2)*	117.87(15)
Dy(1)–O(2)	2.366(4)	Dy(2)–O(10)*	2.392(4)	Dy(1)–O(2)–Dy(2)	112.21(15)
Dy(1)–O(8)*	2.382(4)	Dy(2)–O(8)*	2.495(4)	Dy(1)*–O(8)–Dy(2)*	112.67(14)
Dy(1)–O(5)	2.398(4)	Dy(2)–O(2)	2.524(4)		
Dy(1)–N(4)	2.562(5)	Dy(2)–N(2)	2.540(5)		
Dy(1)–N(5)	2.683(5)	Dy(2)–N(1)	2.549(4)		

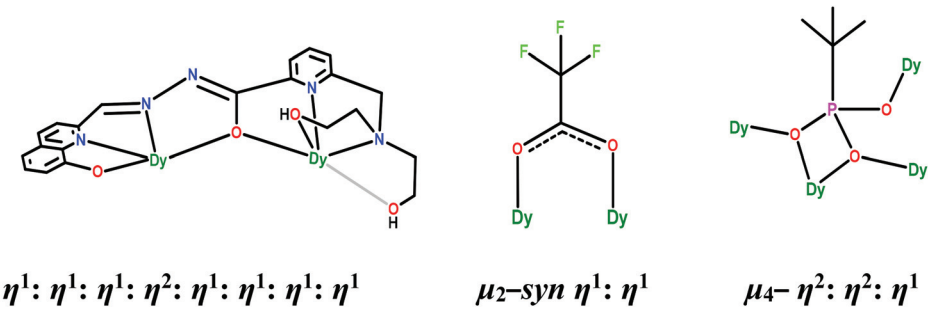

Fig. 3 Binding modes of $[LH_2]^{2-}$, tfa and t-$BuPO_3^{2-}$ ligands in **1**.

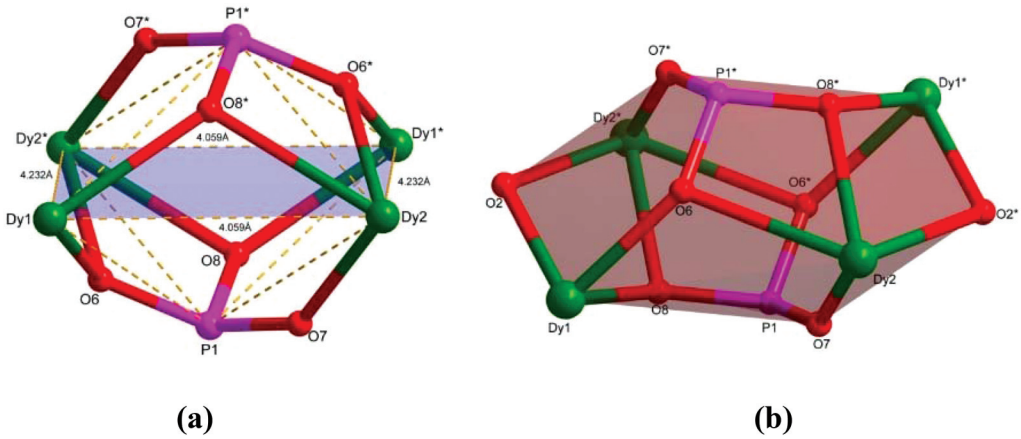

Fig. 4 (a) Tetragonally compressed octahedron core of **1**; (b) rugby ball shaped core of **1**.

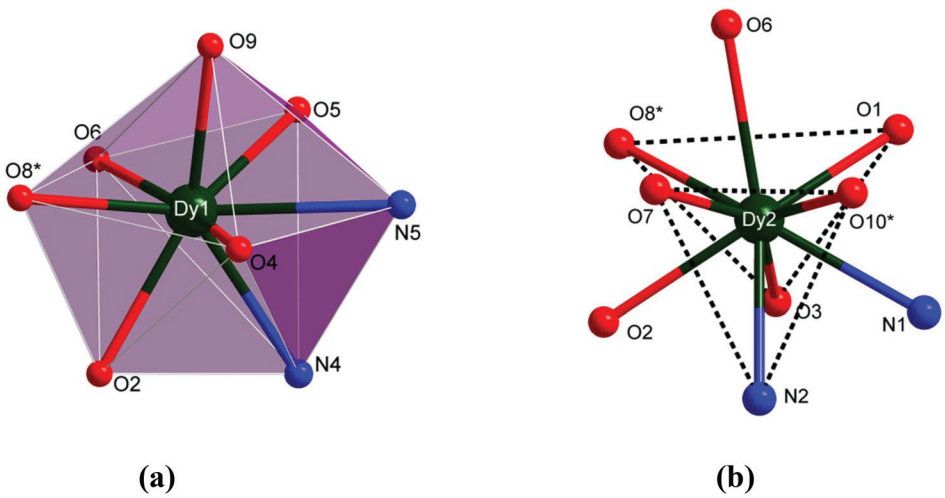

Fig. 5 (a) Distorted triangular dodecahedron geometry around Dy^{III}. (b) Distorted tricapped trigonal prismatic geometry around Dy^{III}.

the range of 2.254–2.651 Å. All the Dy–N bond lengths fall in a very narrow range, 2.539–2.562 Å, except for the Dy–$N_{diethanolamine}$ (2.683 Å) which is slightly longer and consistent with the values found in the literature.[2,8,9] The Dy–$O_{hydrazone}$–Dy bond angle is 112.19° which is almost similar to the Dy–$O8_{phosphonate}$–Dy bond angle, 112.65°, but shorter than the Dy–$O6_{phosphonate}$–Dy bond angle, 117.86°, as anticipated from the larger Dy2–Dy1* distance (Fig. 4a).

Several intramolecular and intermolecular interactions are persistent in complexes **1** and some of these render the formation of remarkable supramolecular motifs which are portrayed in the ESI.†

As mentioned *vide supra* while homometallic Ln_4 complexes with diverse topologies are known, those containing phosphonate ligands are rare.[12a,b] Two such examples were furnished by the research group of Winpenny and coworkers. Interestingly, while $[Dy_4(O_3P^tBu)_2(O_2C^tBu)_4(NO_3)_6(H_2O)_2]^{2-}$ (ref. 12*b*) is a SMM, $[pyH]_4[Dy_4(\mu_3\text{-}OH)(O_3P^tBu)_3(HO_3P^tBu)(O_2C^tBu)_2(NO_3)_6]$[12a] is not.

Magnetic studies

DC studies. The direct-current (dc) magnetic susceptibility measurements of complexes **1–3** were performed in the 2–300 K temperature range and under an applied magnetic field of 0.1 T (Fig. 6). At 0.1 T applied magnetic field, the observed room temperature $\chi_M T$ values 58.25, 47.92 and 32.72 cm^3 K mol^{-1}, for **1–3** respectively, are close to the calculated values of 56.68, 47.25 and 31.5 cm^3 K mol^{-1} for the ground state of the four magnetically non-interacting Dy^{III} ions ($4f^9$, $J = 15/2$, $S = 5/2$, $L = 5$, $g = 4/3$; $^6H_{15/2}$), Tb^{III} ions ($4f^8$, $J = 6$, $S = 3$, $L = 3$, $g = 3/2$; $^7F_6$) and Gd^{III} ions ($4f^7$, $J = 7/2$, $S = 7/2$, $L = 0$, $g = 2.0$; $^8S_{7/2}$) respectively. At 0.1 T applied magnetic field, the $\chi_M T$ product for complexes **1** and **2** steadily decreases from room temperature (300 K) to 50 K (Fig. 6). This arises due to the thermal depopulation of the $|\pm M_J\rangle$ sublevels with a pronounced depopulation effect in **1** compared to **2**. In both the aforementioned complexes, the $\chi_M T$ value drops rapidly below 50 K to reach values of 46.76 and 37.28 cm^3 K mol^{-1} in complexes **1** and **2** respectively at 5 K followed by a further decrease to 43.19 and 32.69 cm^3 K mol^{-1} at 2 K. For complex **3**, under a 0.1 T magnetic field, $\chi_M T$ reduces to 20 K (30.95) with a small increase to 31.39 cm^3 K mol^{-1} at 5 K (Fig. 6). The small plateau at low temperature for complex **1** is maybe due to the intermolecular interaction between the molecules at a very low magnetic field. When a high magnetic field of 1.0 T is applied, this plateau disappears producing a smooth curve (see S10 ESI†).

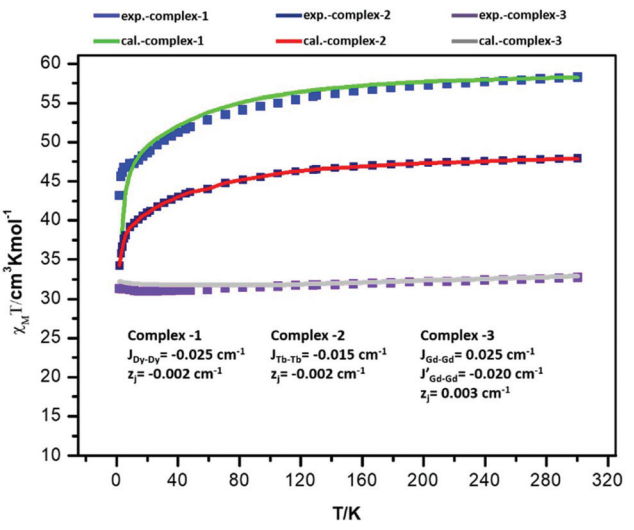

Fig. 6 Temperature-dependent $\chi_M T$ plot for complexes **1–3** where blue, deep blue and violet represent experimental (0.1 T) data for complexes **1–3** respectively, whereas, light green and red imply *ab initio* simulations using only one exchange interaction (J) and constant intermolecular interaction (zJ) of −0.002 cm^{-1} for **1–2** respectively. On the other hand, grey data fitted *via* matrix diagonalization employing PHI programme with zJ = 0.003 cm^{-1} and two isotropic exchange interactions.

Field dependence of the molar magnetization plot in complexes **1** and **2** is shown in the ESI (Fig. S11†). The lack of fitting the magnetization curve into a single master curve for different temperatures indicates the presence of significant anisotropy for complexes **1** and **2**. However, the corresponding solid lines in **3** (completely superimposed with the experimental data) correspond to the best fitted data at zJ = −0.003 cm^{-1} and two isotropic exchange interactions. It is noteworthy that all the J values provided in the graphs correspond to the J^{exch} contribution of the total magnetic interaction (for complexes **1** and **2**).

The decrease in the $\chi_M T$ product upon cooling can be ascribed to the following combined effects: magnetic anisotropy (except complex **3**, in both **1** and **2** owing to highly anisotropic intrinsic Dy^{III} and Tb^{III} ions), intermolecular dipolar magnetic exchange, intramolecular antiferromagnetic exchange and progressive depopulation of the excited state $|\pm M_J\rangle$ stark levels. The above observed decline in the $\chi_M T$ product at higher temperature can be attributed to the larger splitting of the respective ground energy multiplets. In order to evaluate the presence of magnetic anisotropy, field-dependent magnetization measurements were undertaken on three polycrystalline samples of **1** and **2** between 2 and 8 K (2, 4, 6 and 8 K) at fields ranging from 0 to 7 T (Fig. S11†). Magnetization data in **1** and **2** displayed a rapid increment in magnetization below 2 T, beyond which a gradual increase is observed. Magnetization reaches near-saturation slightly below 7 T with 20.60 Nμ_B and 17.23 Nμ_B values at 2 K for **1** and **2** respectively. At all other temperatures magnetization reaches close to saturation under 7 T with 20.55 Nμ_B, 20.42 Nμ_B, and 20.22 Nμ_B at 4, 6, and 8 K respectively for complex **1** (Fig. S11†). Similar behaviour was observed for **2** with near-saturation magnetization values of 17.26 Nμ_B, 17.21 Nμ_B and 17.04 Nμ_B at 4, 6 and 8 K respectively (slightly under 7 T; (Fig. S11†)). The measured values (at all temperatures) for both the complexes are approximately half of the expected value for four weakly coupled lanthanide ions, and can be attributed to the crystal-field effects leading to significant magnetic anisotropy. Contrastingly, measured magnetization for **3** leads to the expected magnetic characteristics. Here, the magnetization reaches close to saturation under 7 T with 28.80 and 28.00 Nμ_B at 2 and 4 K respectively as expected for four weakly coupled isotropic Gd^{III} centres (Fig. 6).

AC studies. With an aim to understand the dynamics of magnetization, alternating current (ac) magnetic susceptibility measurements were undertaken on complexes **1** and **2** (Fig. 7 and S12–S14†). The complexes were measured at 0 and 0.15 T static dc fields (in 3.5 Oe oscillating ac field) within the temperature range of 2–22 K and variable AC frequencies of 111, 311, 511, 711 and 996 Hz. Both the complexes exhibit temperature-independent in-phase (χ') signals in the AC susceptibility

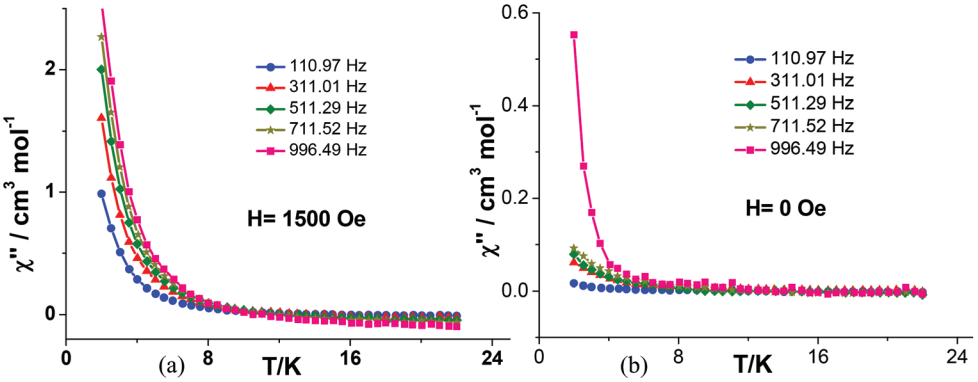

Fig. 7 Temperature-dependent out-of-phase ac susceptibility at (a) 0.15 T dc applied magnetic field for complex **1** and (b) 0 T dc applied magnetic field for complex **1**.

measurements at 0 and 0.15 T magnetic fields. Complex **1** shows frequency- and temperature-dependent out-of-phase (χ'') AC signals at 0 and 0.15 T fields. Frequency- and temperature-dependence of the χ'' component in **1** is evident only at temperatures below 4 K (Fig. 7, S12 and S13†). This is indicative of the possession of SMM characteristics in complex **1** (Fig. 7 and S14†). However, the absence of conspicuous maxima in the χ'' peak (within the temperature/frequency range of our experiments) deters the estimation of the energy barrier for magnetization reversal (U_{eff}) and relaxation time. An extremely weak frequency dependent χ' signal at 0 T field and weak temperature dependence of χ' in 0 and 0.15 T were noted in **2**. Contrarily, a clear lack of frequency-dependent out-of-phase AC signals at 0.15 T field precludes SMM characteristics in **2** (S14†).

Table 2 The CASSCF + RASSI-SO + SINGLE_ANISO computed energy barrier for the magnetization reorientation (U_{cal}) or Δ_{tun} of the four Dy^{III}/Tb^{III} centres along with the main values of the *g*-tensors of ground state KD in complexes **1** and **2**

Complex **1** centres	U_{cal} (cm^{-1})	g_{xx}	g_{yy}	g_{zz}
Dy1	76.7	0.118	0.306	19.118
Dy2	142.1	0.013	0.025	19.698
Dy3	76.7	0.118	0.306	19.063
Dy4	142.1	0.013	0.025	19.728
Complex **2** centres	Δ_{tun} (cm^{-1})			
Tb1	0.04	—	—	17.891
Tb2	0.99	—	—	17.186
Tb3	0.04	—	—	17.871
Tb4	0.99	—	—	17.179

Ab initio calculations

To unravel the nature of the local anisotropy of the Ln^{III} centres and explore the pertinent electronic structural properties, *ab initio* calculations were undertaken on complexes **1–2**. For both the complexes, we have performed two sets of calculations: primarily, using the SINGLE_ANISO program, we have estimated the single-ion magnetic anisotropy of the individual Ln^{III} sites; later, the POLY_ANISO program was utilised to extract the exchange-coupled energy spectra and relevant exchange parameters.

Single-ion analysis

The energy spectrum for eight Kramers doublets of the ground $^6H_{15/2}$ multiplet for the four Dy^{III} ions and *g* tensors of the ground state in compound **1** are shown in Table S4,† with the excited states lying at 3000 cm^{-1}. The ground states of Dy1/Dy3 and Dy2/Dy4 sites exhibit axial type anisotropy with the extent of axiality being predominant for Dy2/Dy4 sites (Tables 2 and S4†). This is verified by g_{xx} = 0.118, g_{yy} = 0.306, g_{zz} = 19.118 and g_{xx} = 0.013, g_{yy} = 0.025, g_{zz} = 19.698 (Fig. 8, yellow dashed line denotes g_{zz} orientation) for Dy1/Dy3 and Dy2/Dy4 sites respectively in their ground state energy multiplets (Tables 2 and S4†). This is due to the larger distortion of Dy1/Dy3 (3.516) sites compared to Dy2/Dy4 (1.583) with respect to the idealised eight coordinated biaugmented trigonal prismatic structure (BTPR) around the Dy^{III} centres. This articulates the similarity between Dy1 and Dy3 magnetic centres as well as Dy2 and Dy4 sites. The ground state g_{zz} value (yellow dashed lines correspond to the alignments of the main anisotropy axes of ground KD in all the four Dy^{III} sites) in all the four centres is close to that expected for a pure $|M_J = \pm 15/2\rangle$ state. In all the Dy^{III} sites, the angle between the g_{zz} directions of the ground and first excited KD lies in the range of ~10–80°. This suggests that relaxation is operative *via* first excited KD in all the four metal centres. The single ion analysis afforded the computed energy barrier (U_{cal}) for magnetization reorientation of 77 and 142 cm^{-1} for two types of non-equivalent Dy^{III} centres (Dy1, Dy3 and Dy2, Dy4) respectively (Fig. S9† for SINGLE_ANISO based computed relaxation mechanism). The negative sign of the B_2^0 crystal field parameters (−1.22, −3.02 for Dy1/Dy3 and Dy2/Dy4 sites respectively) suggests a favourable axial crystal field surrounding the oblate type Dy^{III} ions (Table S5†). A comparatively larger magnitude of B_2^0 for Dy2/Dy4 sites reaffirms our earlier postulate of more axiality (less geometrical distortion).

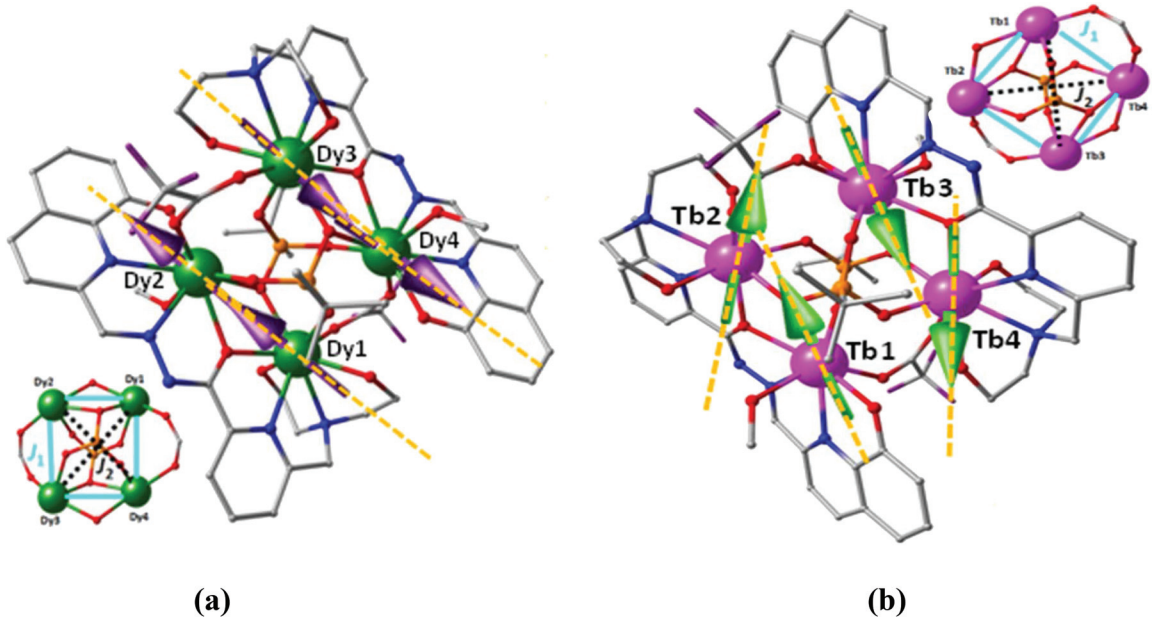

Fig. 8 Crystal structure of complexes (a) **1** and (b) **2** showing main anisotropy axis (yellowish orange dashed lines) on four Dy^{III}/Tb^{III} ions and local magnetization (purple arrows and light green arrows respectively in **1** and **2** respectively) in the ground state. The diagram also illustrates exchange pathways employed for our calculations.

Considerably larger magnitudes of ground state non-axial crystal field parameters (B_2^2, B_2^{-2}) indicate competitiveness between the axial/non-axial terms as well as substantial transverse anisotropy contribution.

The energy spectra for the thirteen energy levels of the ground $^7F_6$ multiplet for the four Tb^{III} ions and g tensors of the ground state in compound **2** are shown in Table S6,† with the excited states lying at 2200 cm^{-1}. Ground (GS) as well as excited state pseudo-doublets show an Ising type anisotropy (17.89 and 17.19 for Tb1/Tb3 and Tb2/Tb4 respectively) for all four metal sites *i.e.* g_{zz} (Fig. 8, yellow dashed lines for orientation of main anisotropy axis for ground pseudo-doublet in all the four Tb^{III} sites) is close (~18) to that expected for a pure $|M_J = \pm 6\rangle$ state. Single ion analysis indicates Δ_{tun} to be 0.04 and 0.99 cm^{-1} within ground pseudo-doublets in non-equivalent Tb^{III} centres (Tb1, Tb3 and Tb2, Tb4) respectively (Tables 2 and S6†). The larger tunnelling gap for Tb2/Tb4 arises due to the larger (3.414) geometrical distortion than that of the Tb1/Tb3 (1.662) site with respect to the ideal BTPR structure. This is further corroborated by a more negative B_2^0 parameter for Tb1/Tb3 (−6.09) than Tb2/Tb4 (−2.00) sites. The substantial tunnel splitting is supported by significant non-axial crystal field parameters for all the four centres (Table S7†). Compared to the Dy4 analogue, where both axial/non-axial crystal field contributions are competitive, the prevalent non-axial term in **2** completely destroys its probability to show SMM behaviour (evident in AC studies). However, **1** is likely to show weak SMM characteristics as also visible in our AC susceptibility studies with the absence of clear maxima in the χ'' peak (frequency dependence).

Relaxation mechanism including exchange coupling for 1 and 2

We have simulated the magnetic interactions between the Ln^{III} ions (Ln = Dy/Tb) *via* incorporating contributions from magnetic dipole–dipole and exchange interactions within an Ising exchange Hamiltonian. We have computed the exchange interaction between the Ln^{III} ions within the Lines model,[13a] with an effective Heisenberg Hamiltonian:[13b,c]

$$\hat{H}_{ex} = -\sum_{i=1}^{3} J_i \cdot S_i \cdot S_{i+1}$$

(here, $J_i = J_i^{dipolar} + J_i^{exch}$; *i.e.* J_i is the total magnetic interaction in combination of calculated $J_i^{dipolar}$ and fitted J_i^{exch} parameters; this summation depicts interaction between all the neighboring Ln^{III} centres). It is worth noting that in the POLY_ANISO[13d,e] code, dipolar contribution is treated explicitly while the exchange part has been estimated from fit to the magnetic data. Magnetic coupling between Ln^{III} ions incorporate contributions from magnetic dipole–dipole and exchange interactions. We have also calculated the exchange spectrum of complexes **1–2** using the POLY_ANISO program. A good agreement between the simulated and experimental magnetic data $\chi_M T$ was (Fig. 6) observed with the parameters J_{Dy-Dy} = −0.025 and J_{Tb-Tb} = −0.015 cm^{-1} at intermolecular interaction (zJ) = −0.002 cm^{-1} for **1** and **2** respectively (Table 3).

Our calculations revealed comparatively stronger ferromagnetic Dy–Dy (even Tb–Tb) dipolar coupling which is in line with conventional literature reports.

Table 3 Parameters of the magnetic interaction between the Dy^{III} and Tb^{III} ions in complexes **1–2**

Complex **1**	J_{Dy-Dy} (cm^{-1})	J_{Tb-Tb} (cm^{-1})
$J_i^{dipolar}$	+0.01	+0.05
J_i^{exch}	−0.025	−0.015
J_{tot}	−0.015	−0.010
zJ	−0.002	−0.002

Exchange coupled analysis reveal no tunneling between the ground state levels for **1** (Fig. S15†). For **2** the magnitude of Δ_{tun} is significantly provoking the relaxation of magnetization through this state itself precluding the SMM behaviour in zero-field and entails the application of magnetic field to show SMM properties[13f,g] (Table 4). In **2**, the first excited exchange doublet lies 1.14 cm^{-1} above the ground state with Δ_{tun} of $\sim10^{-5}$ cm^{-1}. Such a small energy gap between the ground and excited exchange doublets (in conjunction with significant Δ_{tun} within first excited exchange doublets) completely destroys the probability of showing SMM characteristics in **2** even in the presence of an applied field as demonstrated in the experiments (Fig. S15†). Due to very weak antiferromagnetic exchange interactions between the Tb^{III} ions (−0.015 cm^{-1}) exchange-coupling among the metal ions is very weak and expected to be pronounced only at low temperature. Yet as the coupling is weak, the first excited state is very close leading to faster relaxation at lower temperature. At higher temperature single-ion properties are expected to dominate the relaxation mechanism.

Contrarily, the smaller Δ_{tun} value within ground exchange doublets of **1** opens up a channel for magnetization relaxation *via* higher excited multiplets. All the eight low-lying exchange doublets in **1** possess a negligible tunnel splitting of $\sim10^{-9}$ cm^{-1} and expand within the narrow energy window of ~5 cm^{-1}. This infers the probability of relaxation *via* this level and outlines that the computed energy barrier (U_{cal}) for magnetization reorientation is 5.36 cm^{-1} in **1**. This is in agreement with the experimental frequency dependent χ'' AC signal. However, lack of precise maxima in the χ'' peak at the temperature measured deters evaluation of the U_{eff} value and confirms very weak SMM behaviour.

Exchange and SMT investigation of complex 2

To investigate the toroidal nature of complex a more detailed investigation has been performed to plot the low level toroidal states, and has been shown in (Fig. 9). As described in the Lines model approach above, we have extended the analysis to complex **2** and this complex is found to possess stronger dipolar coupling between the Tb^{III} ions which determines the spin projection of the magnetic anisotropy directions in the exchange coupled state, stabilizing the toroidic ground state.

Table 4 Crystal data and structure refinement parameters of **1–3**

	1	**2**	**3**
Formula	$C_{57.7}N_{10}O_{22.3}F_6Dy_4P_2Cl_2H_{76}$	$C_{55.62}H_{70}N_{10}O_{20.38}F_6P_2Cl_2Tb_4$	$C_{58}H_{74}N_{10}O_{24}Gd_4P_2F_6Cl_2$
M/g	2163.32	2087.25	2141.11
Crystal system	Triclinic	Triclinic	Triclinic
Space group	$P\bar{1}$	$P\bar{1}$	$P\bar{1}$
a/Å	12.2754(8)	12.2855	12.294(5)
b/Å	12.9357(8)	12.8600(5)	12.897(5)
c/Å	14.5715(9)	14.6338(6)	14.668(5)
α (°)	112.8160(10)	112.5610(10)	112.258(5)
β (°)	98.8770(10)	99.3550(10)	99.430(5)
γ (°)	108.9790(10)	108.9880(10)	108.876(5)
V/Å^3	1909.6(2)	1906.43(13)	1924.7(13)
Z	1	1	1
ρ_c/g cm^{-3}	1.881	1.818	1.847
μ/mm^{-1}	4.070	3.862	3.601
F(000)	1053.0	1015.0	1044.0
Cryst size (mm^3)	0.11 × 0.09 × 0.08	0.14 × 0.09 × 0.011	0.12 × 0.1 × 0.09
2θ range (°)	4.766 to 50.126	5.468 to 56.756	8.24 to 50.05
Limiting indices	$-12 \le h \le 14$	$-16 \le h \le 16$	$-14 \le h \le 14$
	$-15 \le k \le 15$	$-17 \le k \le 17$	$-15 \le k \le 15$
	$-17 \le l \le 17$	$-19 \le l \le 19$	$-17 \le l \le 17$
Reflns collected	12 451	29 176	23 430
Ind reflns	6718 [R(int) = 0.0249]	9554 [R(int) = 0.0353]	6780 [R(int) = 0.0380]
Completeness to θ (%)	99.9	99.8	100.0
Refinement method	Full-matrix least-squares on F^2	Full-matrix least-squares on F^2	Full-matrix least-squares on F^2
Data/restraints/params	6718/13/496	9554/6/476	6780/3/484
Goodness-of-fit on F^2	1.028	1.048	1.027
Final R indices [$I > 2\theta(I)$]	R_1 = 0.0264	R_1 = 0.0304	R_1 = 0.0284
	wR_2 = 0.0506	wR_2 = 0.0705	wR_2 = 0.0656
R indices (all data)	R_1 = 0.0384	R_1 = 0.0434	R_1 = 0.0394
	wR_2 = 0.0542	wR_2 = 0.0749	wR_2 = 0.0695

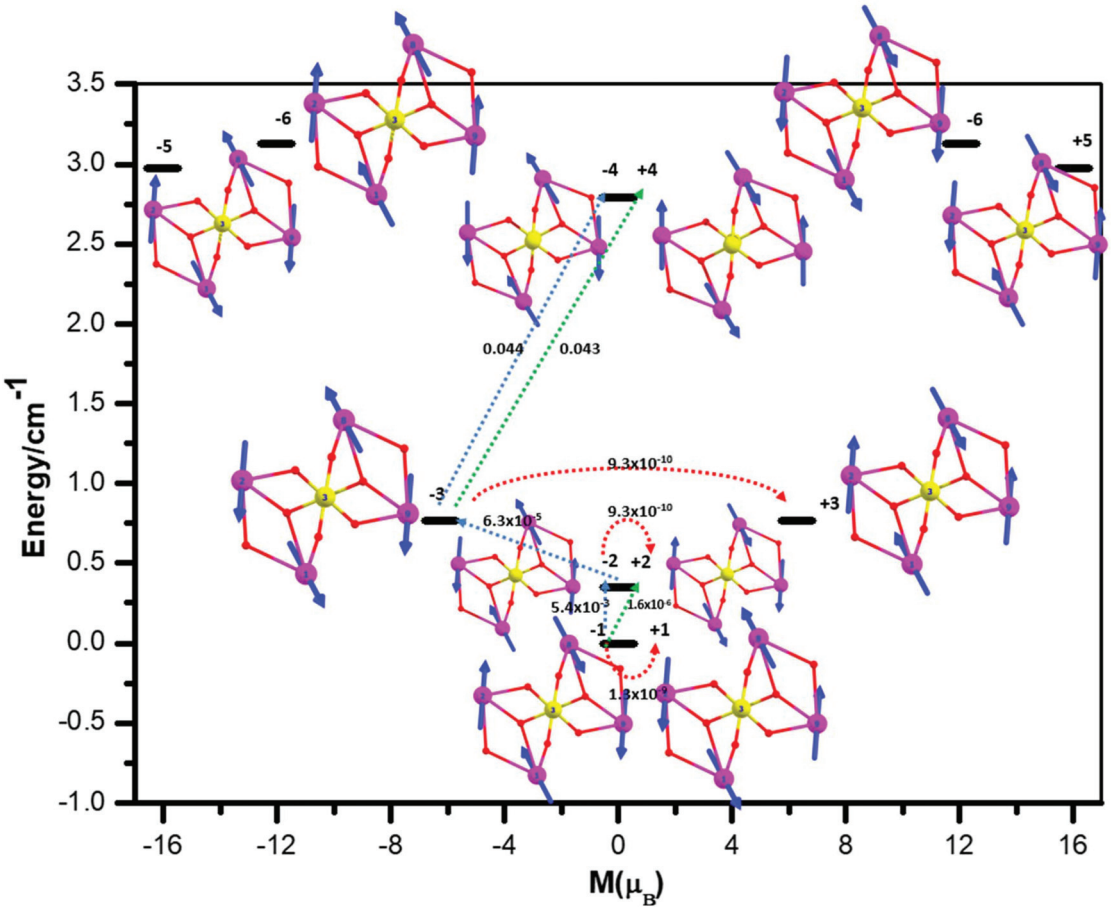

Fig. 9 Low-lying exchange spectrum in complex **2**. The black bold line represents the exchange states as a function of magnetic moment. The red dotted arrows show the tunnelling transitions (energy splitting) within each doublet state, while the green/blue arrows show the possible pathway through TA/Orbach/Raman relaxation. On the corresponding arrows the numbers indicate the transition probability between the two levels. Each energy level is provided with a graphical representation of one of the corresponding non-collinear Ising quantum states, where the blue thick arrows at the Tb^{III} sites indicate the magnetic moment direction in the toroidal form. It has been observed that the ground state is toroidic in nature. Moving to the first and second excited state one anisotropic flip of spin occurs at 0.35 cm^{-1} and 0.76 cm^{-1} destroying the toroidal nature of complex **2**. At more higher level flipping of multiple site occurs destroying the toroidal nature completely.

Conclusions

In summary, we present here a series of tetranuclear lanthanide phosphonates (Ln_4P_2) with a tetragonally compressed octahedron kind of topology, constructed by an aroyl hydrazone based Schiff base ligand, featuring coordination flexibility. Overall, the tetranuclear assemblies contain two types of lanthanide ions; one of them is eight coordinated in a distorted trigonal dodecahedron geometry while the geometry around the other is distorted trigonal prism. Magnetization measurements reveal that room temperature $\chi_M T$ values are in compliance with the expected values. Similarly, field-dependent saturation magnetization values in **1–2** are half of that expected while **3** reproduces the expected saturation magnetization value. *Ab initio* calculations were carried out on the isostructural Ln_4 [Ln = Dy^{III} and Tb^{III}] complexes **1–2** with an aim to profoundly understand the anisotropy orientation, exchange coupled spectrum and toroidal magnetic moments. Complex **1** is SMM but lacks SMT behaviour with a calculated barrier of ~5 cm^{-1}. Complex **2** contrarily shows SMT (net toroidal magnetic moment) behaviour but no SMM characteristics could be detected. In all three complexes, weak antiferromagnetic intramolecular (two types of) magnetic coupling was detected.

Experimental section

Solvents and other general reagents used in this work were purified according to standard procedures.[14] Pyridine-2,6-dicarboxylic acid, sodium borohydride, $DyCl_3{\cdot}6H_2O$, $TbCl_3{\cdot}6H_2O$ and $GdCl_3{\cdot}6H_2O$ were obtained from Sigma Aldrich Chemical Co. and were used as received. Hydrazine hydrate (80%), PBr_3, trifluoroacetic acid, diethanolamine, 2-methyl-8-quinolinol and sodium sulphate (anhydrous) were obtained from S.D. Fine Chemicals, Mumbai, India. Methyl-6-

(hydroxymethyl) picolinate,[2g] methyl 6-(bromomethyl)picolinate,[2g] tertiary butyl phosphonic acid[15] and 8-hydroxyquinoline-2-carbaldehyde[2h] were prepared according to the literature procedures.

Instrumentation

Melting points were measured using a JSGW melting point apparatus and are uncorrected. IR spectra were recorded as KBr pellets on a Bruker Vector 22 FT IR spectrophotometer operating at 400–4000 cm^{-1}. Elemental analyses of the compounds were performed using a Thermoquest CE Instruments CHNS-O, EA/110 model. ESI-MS spectra were recorded on a MICROMASS QUATTRO II triple quadrupole mass spectrometer. ^1H NMR spectra were recorded in $CDCl_3$ and CD_3OD solutions on a JEOL JNM LAMBDA 400 model spectrometer operating at 500 MHz. Chemical shifts are reported in parts per million (ppm) and are referenced with respect to internal tetramethylsilane (^1H).

Magnetic measurements

Magnetic data were measured using a Quantum Design MPMS-XL SQUID magnetometer. All samples were 3 mm diameter pellets molded from ground crystalline samples. Magnetic susceptibility measurements were carried out in the 2–300 K temperature range in a 0.1 or 1 T applied magnetic field, and diamagnetic corrections were considered by Pascal's constants. Isothermal magnetization measurements were undertaken up to 7 T at 2, 4, 6 and in some cases 8 K. The ac susceptibility measurements under different applied static fields were performed using an oscillating ac field of 3.5 Oe and ac frequencies ranging from 10 to 10 000 Hz.

Computational details

The magnetic properties of all the Ln^{III} sites in complexes **1–2** have been studied by fragment *ab initio* calculations. In order to have good illustration of the 3d or 4f ligand field states within a fragment we need to consider the impact of neighbouring metal centres. Owing to the concomitant limitations of MOLCAS (8.0 version)[16] of computing magnetic properties of single paramagnetic metal ion at a time, we have undertaken calculations on individual metal fragments. In both the complexes, four types of calculations have been carried out. For each fragmented calculation, one Ln^{III} ion of interest was kept intact while the other three atoms were replaced by diamagnetic La^{III} ions. All the calculations were carried out on X-ray crystal structures using the ANO-RCC-VDZ basis set as embedded in the MOLCAS suite.

X-ray crystallography

The crystal data for the compounds have been collected on a Bruker SMART CCD diffractometer (MoK_α radiation, λ = 0.71073 Å). The program SMART[17a] was used for collecting frames of data, indexing reflections, and determining lattice parameters, SAINT[17a] for integration of the intensity of reflections and scaling, SADABS[17b] for absorption correction, and SHELXTL[17c,d] for space group and structure determination and least-squares refinements on F^2. The crystal structures were solved and refined by full-matrix least-squares methods against F^2 by using the program SHELXL-2014[17e] using Olex-2 software.[17f] All the non-hydrogen atoms were refined with anisotropic displacement parameters. Hydrogen positions were fixed at calculated positions and refined isotropically. The crystallographic figures have been generated using Diamond 3.1e software.[17g] The crystal data and the cell parameters for compounds **1–3** are summarized in Table 4. Crystallographic data (excluding structure factors) for the structures in this paper have been deposited with the Cambridge Crystallographic Data Centre as supplementary publication no. CCDC 1556047–1556049.†

Synthesis

Methyl 6-((bis(2-hydroxyethyl)amino)methyl)picolinate. To a solution of diethanolamine (1.912 g, 18.2 mmol) in dry THF (60 mL), triethylamine (7.18 mL, 54.16 mmol) was added dropwise and the resulting colourless solution was stirred at room temperature for 20 minutes. Then, methyl 6-(bromomethyl) picolinate (4.2 g, 18.2 mmol) in dry THF (40 mL) was added dropwise over a period of 30 minutes under vigorous stirring. After that the solution was stirred for a further period of 24 hours at room temperature to afford a heavy white sticky precipitate which was filtered. The colourless filtrate was evaporated to obtain a hazy light yellow coloured oil which was dissolved in dichloromethane (40 mL) followed by washing with water (40 mL × 2) and brine solution (30 mL × 2). The combined organic extracts were dried (anhydrous sodium sulphate) and the solvent was removed to afford a yellow oil. Yield: 3.87 g, 83.42%. ^1H NMR (500 MHz, $CDCl_3$, δ, ppm): 2.84 (t, 4H, $-NCH_2$), 3.57 (t, 4H, $-CH_2O$), 3.94 (s, 3H, OMe), 3.97 (s, 2H, NCH_2), 5.28 (s, 1H, –OH), 7.43 (d, 1H, Py–H), 7.79 (t, 1H, Py–H), 8.01 (d, 1H, Py–H). Anal. calcd for $C_{12}H_{18}N_2O_4$ (254.28): C, 56.68; H, 7.13; N, 11.02. Found: C, 56.37; H, 6.58; N, 11.51. ESI-MS, m/z: $(M + H)^+$: 255.07.

Methyl 6-((bis(2-hydroxyethyl)amino)methyl)picolinohydrazide. 6-((Bis(2-hydroxyethyl)amino)methyl)picolinate (3.6 g, 14.16 mmol) was taken in ethanol (30 mL) and added dropwise to an ethanolic solution (40 mL) of hydrazine hydrate (3.54 g, 70.8 mmol) at room temperature. The reaction mixture was heated under reflux for 5 hours. Then, the solution was allowed to cool to room temperature and concentrated to 20 mL *in vacuo* before being kept in a refrigerator overnight. A white precipitate formed was filtered, washed with cold ethanol 2–3 times and dried. Yield: 3.21 g, 88.93%. Anal. calcd for $C_{11}H_{18}N_4O_3$ (254.13): C, 51.96; H, 7.13; N, 22.03. Found: C, 52.32; H, 7.52; N, 22.37. Mp: 155 °C; ^1H NMR (500 MHz, CD_3OD, δ, ppm): 2.71 (t, 4H, $-NCH_2$), 3.64 (t, 4H, $-CH_2O$), 3.90 (s, 2H, $-NCH_2$), 7.64 (d, 2H, Py–H), 7.87 (t, 1H, Py–H). ESI-MS, m/z: $(M + H)^+$: 255.14.

6-((Bis(2-hydroxyethyl)amino)methyl)-*N*′-((8-hydroxyquinolin-2-yl)methylene)picolinohydrazide (LH_4). To an ethanolic solution (40 mL) of methyl-6-((bis(2-hydroxyethyl)amino) methyl)picolinohydrazide (1.5 g, 5.9 mmol) under stirring, 8-hydroxyquinoline-2-carbaldehyde (1.02 g, 5.9 mmol) also dis-

solved in ethanol (20 mL) was added dropwise at room temperature over a period of 30 minutes. The resulting orange yellow solution was heated under reflux for 4 hours. Then, the turbid solution was concentrated *in vacuo* to 20 mL and kept in a refrigerator overnight. The yellow precipitate obtained was filtered, washed twice with cold ethanol and diethyl ether and dried. Yield: 1.96 g (81.2%). Anal. calcd for $C_{21}H_{23}N_5O_4$ (409.17): C, 61.60; H, 5.66; N, 17.10 Found: C, 61.07; H, 5.73; N, 17.47. Mp: 164 °C. ^{1}H NMR (500 MHz, CD_3OD, δ, ppm): 2.81 (t, 4H, NCH_2), 3.70 (t, 4H, CH_2O), 4.00 (s, 2H, NCH_2), 4.52 (br, 1H, CH_2OH), 5.46 (s, 1H, OH), 7.11 (d, 1H, Ar–H), 7.36 (d, 1H, Ar–H), 7.45 (t, 1H, Ar–H), 7.70 (d, 1H, Py–H), 7.96 (t, 1H, Py–H), 8.1 (d, 1H, Py–H), 8.26–8.29 (m, 2H, Ar–H), 8.68 (1H, imine-H). FT-IR (KBr) cm^{-1}: 3395 (s), 3231 (s), 2957 (w), 2870 (w), 2807 (m), 1676 (s), 1583 (m), 1567 (m), 1506 (s), 1451 (m), 1463 (s), 1403 (s), 1261 (s), 1244 (m), 1210 (m), 1088 (s), 1036 (m), 993 (s), 941 (m), 922 (m), 871 (w), 848 (s), 763 (w), 725 (w) ESI-MS, *m*/*z*: $(M + H)^+$: 410.17.

General synthetic procedure for the preparation of complexes 1–3

The synthesis of compounds, **1–3**, were carried out by following the same procedure outlined below.

To a stirred solution of LH_4 (0.041 g, 0.1 mmol) in methanol (40 mL), $LnCl_3{\cdot}6H_2O$ (0.2 mmol) was added to give an intense red coloured solution which was allowed to stir for 20 minutes at room temperature. Then, $H_2O_3P^tBu$ (0.014 g, 0.1 mmol) was added followed by the addition of triethylamine (0.04 mL, 0.3 mmol). The reaction mixture was allowed to stir for further 15 minutes. At this stage, trifluoroacetic acid (0.011 g, 0.1 mmol) was added dropwise along with the addition of further triethylamine (0.014 mL, 0.1 mmol) to afford a dark red solution which was stirred overnight at room temperature. The reaction mixture was filtered and the solvent was removed *in vacuo* affording a reddish oily mass which was washed twice with diethyl ether and dried. This was further dissolved in methanol and diethyl ether was slowly allowed to diffuse. Block-shaped crystals suitable for X-ray diffraction were obtained after 9 days. The details of each reaction and characterization data of these complexes (**1–3**) are given below.

$[Dy_4(LH_2)_2(O_3P^tBu)_2(\mu_2\text{-}\eta^1\eta^1tfa)_2]{\cdot}2Cl{\cdot}2MeOH{\cdot}2H_2O$ (1). Quantities: LH_4 (0.041 g, 0.1 mmol), $DyCl_3{\cdot}6H_2O$ (0.075 g, 0.2 mmol), HO_3P^tBu (0.014 g, 0.1 mmol), tfa (0.011 g, 0.1 mmol), Et_3N (0.054 mL, 0.4 mmol). Yield: 0.071 g, 32.56% (based on Dy^{III}). Mp: >250 °C (d). IR (KBr) cm^{-1}: 3396 (br), 2953 (br), 1690 (s), 1619 (w), 1591 (w), 1556 (s), 1529 (s), 1505 (w), 1456 (w), 1429 (w), 1392 (s), 1338 (s), 1306 (w), 1274 (s), 1209 (s), 1142 (s), 1103 (w), 1057 (w), 1010 (w), 997 (w), 975 (s), 938 (w), 901 (w), 835 (w), 795 (w), 770 (w), 758 (w), 720 (s), 741 (w), 656 (w), 575 (w), 505 (s). Anal. calcd for $C_{58}H_{76}Cl_2Dy_4F_6N_{10}O_{24}P_2$ (2194.13): C, 31.75; H, 3.49; N, 6.38. Found: C, 31.91; H, 3.28; N, 6.44. ESI-MS *m*/*z* ion: 1872.142, $(C_{51}H_{64}Dy_4N_{10}O_{15}P_2 + K^+ + 2H_2O + MeOH - 4H^+)^+$.

$[Tb_4(LH_2)_2(O_3P^tBu)_2(\mu_2\text{-}\eta^1\eta^1tfa)_2]{\cdot}2Cl{\cdot}2MeOH{\cdot}2H_2O$. Quantities: LH_4 (0.041 g, 0.1 mmol), $TbCl_3{\cdot}6H_2O$ (0.074 g, 0.2 mmol), HO_3P^tBu (0.014 g, 0.1 mmol), tfa (0.011 g, 0.1 mmol), Et_3N (0.054 mL, 0.4 mmol). Yield: 0.069 g, 31.76% (based on Tb^{III}). Mp: >250 °C (d). IR (KBr) cm^{-1}: 3391 (br), 2950 (br), 1695 (s), 1613 (w), 1595 (w), 1557 (w), 1529 (s), 1503 (w), 1451 (w), 1427 (w), 1388 (s), 1331 (s), 1303 (w), 1279 (s), 1212 (s), 1140 (s), 1103 (w), 1052 (w), 1007 (w), 992 (w), 971 (s), 942 (w), 901 (w), 833 (w), 799 (w), 771 (w), 756 (w), 721 (s), 746 (w), 654 (w), 572 (w), 501 (s). Anal. calcd for $C_{58}H_{78}Cl_2F_6N_{10}O_{24}P_2Tb_4$ (2181): C, 31.93; H, 3.60; N, 6.42. Found: C, 32.33; H, 3.78; N, 6.11. ESI-MS *m*/*z* ion: 1789.046 $(C_{51}H_{64}N_{10}O_{15}P_2Tb_4 + K^+ - 4H^+)^+$.

$[Gd_4(LH_2)_2(O_3P^tBu)_2(\mu_2\text{-}\eta^1\eta^1tfa)_2]{\cdot}2Cl{\cdot}2MeOH{\cdot}2H_2O$. Quantities: LH_4 (0.041 g, 0.1 mmol), $GdCl_3{\cdot}6H_2O$ (0.075 g, 0.2 mmol), HO_3P^tBu (0.014 g, 0.1 mmol), tfa (0.011 g, 0.1 mmol), Et_3N (0.054 mL, 0.4 mmol). Yield: 0.067 g, 31% (based on Gd^{III}). Mp: >250 °C (d). IR (KBr) cm^{-1}: 3399 (br), 2954 (br), 1692 (s), 1611 (w), 1594 (w), 1553 (s), 1526 (s), 1501 (w), 1459 (w), 1433 (w), 1397 (s), 1339 (s), 1301 (w), 1273 (s), 1212 (s), 1147 (s), 1109 (w), 1053 (w), 1013 (w), 991 (w), 978 (s), 931 (w), 895 (w), 830 (w), 797 (w), 767 (w), 758 (w), 720 (s), 748 (w), 651 (w), 574 (w), 503 (s). Anal. calcd for $C_{58}H_{74}Cl_2F_6Gd_4N_{10}O_{24}P_2$ (2171.11): C, 32.09; H, 3.44; N, 6.45. Found: C, 31.81; H, 3.50; N, 6.69. ESI-MS *m*/*z* ion: 1886.105, $(C_{52}H_{60}F_3Gd_4N_{10}O_{16}P_2 + H_2O + CH_3CN - 2H^+)^+$.

Conflicts of interest

There are no conflicts to declare.

Acknowledgements

We thank the Department of Science and Technology (DST), India, for financial support, including support for a Single Crystal CCD X-ray Diffractometer facility at IIT-Kanpur. V. C. is grateful to the DST for a J. C. Bose fellowship. GR thanks the SERB (EMR/2014/000247) for the financial support. TG and AS thank the UGC for a fellowship.

References

1 (*a*) S. V. Eliseeva and C. G. Bunzli, *Chem. Soc. Rev.*, 2010, **39**, 189–227; (*b*) M. C. Heffern, L. M. Matosziuk and T. J. Meade, *Chem. Rev.*, 2014, **114**, 4496–4539; (*c*) R. A. Layfield, *Organometallics*, 2014, **33**, 1084–1099; (*d*) M. Feng and M.-L. Tong, *Chem. – Eur. J.*, 2018, **24**, 7574–7594; (*e*) J.-L. Liu, Y.-C. Chen and M.-L. Tong, *Chem. Soc. Rev.*, 2018, **47**, 2431–2453.

2 (*a*) S. Das, S. Hossain, A. Dey, S. Biswas, J.-P. Sutter and V. Chandrasekhar, *Inorg. Chem.*, 2014, **53**, 5020–5028; (*b*) J. J. Baldoví, S. C. Serra, J. M. C. Juan, E. Coronado, A. Gaita-Ariño and A. Palii, *Inorg. Chem.*, 2012, **51**, 12565–12574; (*c*) S. Biswas, A. Mondal and S. Konar, *Inorg. Chem.*, 2016, **55**, 2085–2090; (*d*) S. P. Bera, A. Roy, S. Mondal, B. Dey, A. Santra and S. Konar, *Dalton Trans.*, 2018, **47**, 15405–15415; (*e*) F. Pointillart, J.-K. Ou-Yang, G. F. Garcia,

V. Montigaud, J. F. Gonzalez, R. Marchal, L. Favereau, F. Totti, J. Crassous, O. Cador, L. Ouahab and B. L. Guennic, *Inorg. Chem.*, 2019, **58**, 52–56; (*f*) K. Katoh, T. Morita, N. Yasuda, W. Wernsdorfer, Y. Kitagawa, B. K. Breedlove and M. Yamashita, *Chem. – Eur. J.*, 2018, **24**, 15522–15528; (*g*) S. Biswas, S. Das, T. Gupta, S. K. Singh, M. Pissas, G. Rajaraman and V. Chandrasekhar, *Chem. – Eur. J.*, 2016, **22**, 18532–18550; (*h*) S. Biswas, S. Das, J. Acharya, V. Kumar, J. V. Leusen, P. Kögerler, J. M. Herrera, E. Colacio and V. Chandrasekhar, *Chem. – Eur. J.*, 2017, **23**, 5154–5170; (*i*) B. S. Dolinar, D. I. Alexandropoulos, K. R. Vignesh, T.' A. James and K. R. Dunbar, *J. Am. Chem. Soc.*, 2018, **140**, 908–911.

3 (*a*) D. N. Woodruff, R. E. P. Winpenny and R. A. Layfield, *Chem. Rev.*, 2013, **113**, 5110–5148; (*b*) A. Dey, P. Kalita and V. Chandrasekhar, *ACS Omega*, 2018, **3**, 9462–9475; (*c*) F.-S. Guo, B. M. Day, Y.-C. Chen, M.-L. Tong, A. Mansikkamäki and R. A. Layfield, *Science*, 2018, **362**, 1400–1403.

4 (*a*) N. F. Chilton, C. A. P. Goodwin, D. P. Mills and R. E. P. Winpenny, *Chem. Commun.*, 2015, **51**, 101–103; (*b*) R. J. Blagg, L. Ungur, F. Tuna, J. Speak, P. Comar, D. Collison, W. Wernsdorfer, E. J. L. McInnes, L. F. Chibotaru and R. E. P. Winpenny, *Nat. Chem.*, 2013, **5**, 673–678; (*c*) C. B. P. Finn, R. Orbach and W. P. Wolf, *Proc. Phys. Soc., London*, 1961, **77**, 261–268.

5 (*a*) L. F. Chibotaru, L. Ungur and A. Soncini, *Angew. Chem., Int. Ed.*, 2008, **47**, 4126–4129; (*b*) L. Ungur, S.-Y. Lin, J. Tang and L. F. Chibotaru, *Chem. Soc. Rev.*, 2014, **43**, 6894–6905; (*c*) G. Novitchi, G. Pilet, L. Ungur, V. V. Moshchalkov, W. Wernsdorfer, L. F. Chibotaru, D. Luneau and A. K. Powell, *Chem. Sci.*, 2012, **3**, 1169–1176; (*d*) K. R. Vignesh, S. K. Langley, A. Swain, B. Moubaraki, M. Damjanović, W. Wernsdorfer, G. Rajaraman and K. S. Murray, *Angew. Chem., Int. Ed.*, 2018, **57**, 779–784; (*e*) T. Kaelberer, V. A. Fedotov, N. Papasimakis, D. P. Tsai and N. I. Zheludev, *Science*, 2010, **330**, 1510–1512.

6 (*a*) J. Zhang, Y. Man, W. Liu, B. Liu and Y. Dong, *Dalton Trans.*, 2019, **48**, 2560–2563; (*b*) P. Richardson, T. J. Hsu, C. J. Kuo, R. J. Holmberg, B. Gabidullin, M. Rouzieres, R. Clerac, M. Murugesu and P.-H. Lin, *Dalton Trans.*, 2018, **47**, 12847–12851; (*c*) T. Gamer, M. Y. Lan, P. W. Roesky, A. K. Powell and R. Clerac, *Inorg. Chem.*, 2008, **47**, 6581–6583; (*d*) B. Hussain, D. Savard, J. T. Burchell, W. Wernsdorfer and M. Murugesu, *Chem. Commun.*, 2009, 1100–1102; (*e*) X. Zheng, L.-P. Jin and S. Gao, *Inorg. Chem.*, 2004, **43**, 1600–1602; (*f*) T. Kajiwara, H. Wu, T. Ito, N. Iki and S. Miyano, *Angew. Chem., Int. Ed.*, 2004, **43**, 1832–1836; (*g*) G.-F. Xu, P. Gamez and J. Tang, *Dalton Trans.*, 2010, **39**, 4353–4357; (*h*) G. Westin, L. M. Kritikos and A. Caneschi, *Chem. Commun.*, 2003, 1012–1013; (*i*) P. Andrews, C. B. H. Fraser, P. C. Junk, M. Massi and P. W. Roesky, *Dalton Trans.*, 2007, 5651–5654; (*j*) A. S. R. Chesman, D. R. Turner, B. Moubaraki, K. S. Murray, G. B. Deacon and S. R. Batten, *Chem. – Eur. J.*, 2009, **15**, 5203–5207; (*k*) R. Wang, D. Song and S. Wang, *Chem. Commun.*, 2002, 368–369; (*l*) R. Wang, Z. Zheng, T. Jin and R. J. Staples, *Angew. Chem., Int. Ed.*, 1999, **38**, 1813–1815; (*m*) X. Gu and D. Xue, *Inorg. Chem.*, 2007, **46**, 3212–3216.

7 (*a*) S. Y. Lin and J. Tang, *Polyhedron*, 2014, **83**, 185–196; (*b*) K. Zhang, G.-P. Li, V. Montigaud, O. Cador, B. L. Guennic, J. Tang and Y.-Y. Wang, *Dalton Trans.*, 2019, **48**, 2135–2141.

8 (*a*) M. U. Anwar, L. K. Thompson, L. N. Dawe, F. Habibb and M. Murugesu, *Chem. Commun.*, 2012, **48**, 4576–4578; (*b*) S. Biswas, S. Das, J. V. Leusen, P. Kögerler and V. Chandrasekhar, *Eur. J. Inorg. Chem.*, 2014, 4159–4167; (*c*) S. Biswas, S. Das, S. Hossain, A. K. Bar, J. P. Sutter and V. Chandrasekhar, *Eur. J. Inorg. Chem.*, 2016, 4683–4692; (*d*) G. F. Garcia, D. Guettas, V. Montigaud, P. Larini, R. Sessoli, F. Totti, O. Cador, G. Pilet and B. L. Guennic, *Angew. Chem., Int. Ed.*, 2018, **52**, 17335–17339; (*e*) Y. Bi, X.-T. Wang, W. Liao, X. Wang, R. Deng, H. Zhang and S. Gao, *Inorg. Chem.*, 2009, **48**, 11743–11747; (*f*) S. Xue, Y.-N. Guo, L. Zhao, P. Zhang and J. Tang, *Dalton Trans.*, 2014, **43**, 1564–1570; (*g*) V. Chandrasekhar, S. Hossain, S. Das, S. Biswas and J.-P. Sutter, *Inorg. Chem.*, 2013, **52**, 6346–6353; (*h*) J. Goura, J. P. S. Walsh, F. Tuna and V. Chandrasekhar, *Inorg. Chem.*, 2014, **53**, 3385–3395; (*i*) Y.-N. Guo, G.-F. Xu, P. Gamez, L. Zhao, S.-Y. Lin, R. Deng, J. Tang and H.-J. Zhang, *J. Am. Chem. Soc.*, 2010, **132**, 8538–8539; (*j*) J. Acharya, S. Biswas, J. van Leusen, P. Kumar, V. Kumar, R. S. Narayanan, P. Kögerler and V. Chandrasekhar, *Cryst. Growth Des.*, 2018, **18**, 4004–4016.

9 (*a*) S. Das, A. Dey, S. Biswas, E. Colacio and V. Chandrasekhar, *Inorg. Chem.*, 2014, **53**, 3417–3426; (*b*) H. Tian, B.-L. Wang, J. Lu, H.-T. Liu, J. Su, D. Li and J. Dou, *Chem. Commun.*, 2018, **54**, 12105–12108.

10 (*a*) P.-H. Lin, T. J. Burchell, L. Ungur, L. F. Chibotaru, W. Wernsdorfer and M. Murugesu, *Angew. Chem., Int. Ed.*, 2009, **48**, 9489–9492.

11 (*a*) J. Goura and V. Chandrasekhar, *Chem. Rev.*, 2015, **115**, 6854–6965; (*b*) J. A. Sheikh, H. S. Jena, A. Clearfield and S. Konar, *Acc. Chem. Res.*, 2016, **49**, 1093–1103; (*c*) F.-M. Zhang, L.-Z. Dong, J.-S. Qin, W. Guan, J. Liu, S.-L. Li, M. Lu, Y.-Q. Lan, Z.-M. Su and H.-C. Zhou, *J. Am. Chem. Soc.*, 2017, **139**, 6183–6189; (*d*) S.-S. Bao, G. K. H. Shimizu and L.-M. Zheng, *Coord. Chem. Rev.*, 2019, **378**, 577–594; (*e*) S. K. Gupta, S. K. Langley, K. Sharma, K. S. Murray and R. Murugavel, *Inorg. Chem.*, 2017, **56**, 3946–3960; (*f*) S. K. Gupta, G. A. Bhat and R. Murugavel, *Inorg. Chem.*, 2017, **56**, 9071–9083; (*g*) S. K. Gupta, A. A. Dar, T. Rajeshkumar, S. Kuppuswamy, S. K. Langley, K. S. Murray, G. Rajaraman and R. Murugavel, *Dalton Trans.*, 2015, **44**, 5961–5965; (*h*) Y.-Z. Zheng, M. Evangelisti, F. Tuna and R. E. P. Winpenny, *J. Am. Chem. Soc.*, 2012, **134**, 1057; (*i*) Y.-Z. Zheng, M. Evangelisti and E. P. Winpenny, *Chem. Sci.*, 2011, **2**, 99.

12 (*a*) K. H. Zangana, E. M. Pineda and R. E. P. Winpenny, *Dalton Trans.*, 2014, **43**, 17101–17107; (*b*) K. H. Zangana, E. M. Pineda and R. E. P. Winpenny, *Dalton Trans.*, 2015,

44, 12522–12525; (*c*) K. H. Zangana, E. M. Pineda, J. Schnack and R. E. P. Winpenny, *Dalton Trans.*, 2013, **42**, 14045–14048; (*d*) K. H. Zangana, E. M. Pineda, E. J. L. McInnes, J. Schnack and R. E. P. Winpenny, *Chem. Commun.*, 2014, **50**, 1438–1440.

13 (*a*) M. E. Lines, *J. Chem. Phys.*, 1971, **55**, 2977–2984; (*b*) L. F. Chibotaru, L. Ungur and A. Soncini, *Angew. Chem., Int. Ed.*, 2008, **47**, 4126–4129; (*c*) L. Ungur, W. V. d. Heuvela and L. F. Chibotaru, *New J. Chem.*, 2009, **33**, 1224–1228; (*d*) L. Ungur and L. F. Chibotaru, *POLY_ANISO program*, KU Leuven, Belgium, 2007; (*e*) L. F. Chibotaru and L. Ungur, *The computer programs SINGLE_ANISO and POLY_ANISO*, University of Leuven, Belgium, 2006; (*f*) L. F. Chibotaru, L. Ungur, C. Aronica, H. Elmoll, G. Pilet and D. Luneau, *J. Am. Chem. Soc.*, 2008, **130**, 12445–12455; (*g*) K. C. Mondal, A. Sundt, Y. Lan, G. E. Kostakis, O. Waldmann, L. Ungur, C. E. Anson and A. K. Powell, *Angew. Chem., Int. Ed.*, 2012, **51**, 7550–7554.

14 (*a*) *Vogel's Textbook of Practical Organic Chemistry*, ed. B. S. Furniss, A. J. Hannaford, P. W. G. Smith and A. R. Tatchell, ELBS and Longman, London, 5th edn, 1989; (*b*) D. B. G. Williams and M. Lawton, *J. Org. Chem.*, 2010, **75**, 8351–8354; (*c*) X. Zeng, D. Coquiére, A. Alenda, E. Garrier, T. Prangé, Y. Li, O. Reinaud and I. Jabin, *Chem. – Eur. J.*, 2006, **12**, 6393–6402.

15 P. C. Crofts and G. M. Kosolapoff, *J. Am. Chem. Soc.*, 1953, **75**, 3379–3383.

16 (*a*) F. Aquilante, J. Autschbach, R. K. Carlson, L. F. Chibotaru, M. G. Delcey, L. De Vico, I. F Galván, N. Ferré, L. M. Frutos, L. Gagliardi, M. Garavelli, A. Giussani, C. E. Hoyer, G. Manni, H. Lischka, D. Ma, P. Å. Malmqvist, T. Müller, A. Nenov, M. Olivucci, T. B. Pedersen, D. Peng, F. Plasser, B. Pritchard, M. Reiher, I. Rivalta, I. Schapiro, J. Segarra-Martí, M. Stenrup, D. G. Truhlar, L. Ungur, A. Valentini, S. Vancoillie, V. Veryazov, V. P. Vysotskiy, O. Weingart, F. Zapata and R. Lindh, Molcas 8, *J. Comput. Chem.*, 2016, **37**, 506–541; (*b*) F. Aquilante, L. De Vico, N. Ferre, G. Ghigo, P. A. Malmqvist, P. Neogrady, T. B. Pedersen, M. Pitonak, M. Reiher, B. O. Roos, L. Serrano-Andres, M. Urban, V. Veryazov and R. Lindh, Software News and Update MOLCAS 7: The Next Generation, *J. Comput. Chem.*, 2010, **31**, 224–247; (*c*) J. A. Duncan, Molcas 7.2., *J. Am. Chem. Soc.*, 2009, **131**, 2416–2416; (*d*) G. Karlstrom, R. Lindh, P. A. Malmqvist, B. O. Roos, U. Ryde, V. Veryazov, P. O. Widmark, M. Cossi, B. Schimmelpfennig, P. Neogrady and L. Seijo, MOLCAS, *Comput. Mater. Sci.*, 2003, **28**, 222–239; (*e*) V. Veryazov, P. O. Widmark, L. Serrano-Andres, R. Lindh and B. O. Roos, 2MOLCAS, *Int. J. Quantum Chem.*, 2004, **100**, 626–635.

17 (*a*) *SMART & SAINT Software Reference manuals, Version 6.45*, Bruker Analytical X-ray Systems, Inc., Madison, WI, 2003; (*b*) G. M. Sheldrick, *SADABS, a software for empirical absorption correction, Ver. 2.05*, University of Göttingen, Göttingen, Germany, 2002; (*c*) *SHELXTL Reference Manual, Ver. 6.1*, Bruker Analytical X-ray Systems, Inc., Madison, WI, 2000; (*d*) G. M. Sheldrick, *SHELXTL, Ver. 6.12*, Bruker AXS Inc., WI. Madison, 2001; (*e*) G. M. Sheldrick, *Acta Crystallogr., Sect. A: Found. Crystallogr.*, 2008, **64**, 112–122; (*f*) O. V. Dolomanov, L. J. Bourhis, R. J. Gildea, J. A. K. Howard and H. Puschmann, *J. Appl. Crystallogr.*, 2009, **42**, 339–341; (*g*) K. Bradenburg, *Diamond, Ver. 3.1eM*, Crystal Impact GbR, Bonn, Germany, 2005.

